Journal of Innovative Optical Health Sciences
Vol. 4, No. 3 (2011) 309−323

DOI: 10.1142/S1793545811001435

OPTIMIZATION OF DESIGN PARAMETERS FOR FLUORESCENCE LAMINAR OPTICAL TOMOGRAPHY

CHAO-WEI CHEN and YU CHEN*
Fischell Department of Bioengineering and Electrical and Computer Engineering
2218 Jeong H. Kim Building, University of Maryland
College Park, MD 20742, USA
**yuchen@umd.edu*

Accepted 10 March 2011

Laminar optical tomography (LOT) is a mesoscopic tomographic imaging technique ranging between confocal microscopy and diffuse optical tomography (DOT). Fluorescence LOT (FLOT) provides depth-resolved molecular information with 100−200 μm resolution over 2−3 mm depth. In this study, we use Monte Carlo simulation and singular-value analysis (SVA) to optimize the source-detector configurations for potential enhancement of FLOT imaging performance. The effects of different design parameters, including source incidence and detector collection angles, detector number, and sampling density, are presented. The results indicate that angled incidence/detection configuration might improve the imaging resolution and depth sensitivity, especially for low-scattering medium. Increasing the number of detectors and the number of scanning steps will also result in enhanced imaging performance. We also demonstrate that the optimal imaging performance depends upon the background scattering coefficient. Our result might provide an optimization strategy for FLOT or LOT experimental setup.

Keywords: Laminar optical tomography (LOT); fluorescence laminar optical tomography (FLOT); singular value analysis (SVA); image reconstruction.

1. Introduction

Laminar optical tomography (LOT) has been developed to perform depth-resolved functional imaging with ∼100−200 μm resolution and ∼2−3 mm depth.[1,2] LOT is an extension of confocal microscopy using multiple-detector design to capture photons traveling through different depths, and the image is obtained through transport-based reconstruction.[1−3] Fluorescence LOT (FLOT) provides depth-resolved molecular information using either endogenous fluorophores or exogenous contrast agents.[4−6] FLOT has been demonstrated on depth-resolved imaging of cardiac transmural electrical propagation[4] and subsurface breast cancer xenografts.[7] The resolution of FLOT (and LOT) is typically ∼100−200 μm. However, the point spread function (PSF) enlarges while the object locates deeper.[2,7] Our previous measurement indicates an axial PSF of ∼300−400 μm at ∼1 mm depth.[7]

Optimization of FLOT imaging configuration, namely, the source and detector arrangements, may result in improvement in imaging performance. The

*Corresponding author.

depth selectivity of FLOT system could be controlled by the source-detector configuration. Previous work in optical spectroscopy suggests that using angled illumination-collection fiber design (oblique illumination/collection) will enhance the depth selectivity of epithelium tissues.[8–12] This novel approach can be implemented in FLOT imaging to vary the depth selectivity and potentially enhance the depth resolution of image reconstruction. Furthermore, detector (or sampling) density is also an important factor regulating the resolution in diffuse optical tomography (DOT).[13] Through optimization, one can use a reasonable number of detectors to acquire maximal amount of information, thereby reaching an optimal tradeoff between imaging performance and cost.

In this study, we use Monte Carlo simulation to investigate the effects of different design parameters on FLOT imaging performance. The parameters investigated here include the incident and detection angle of source and detectors, the detector numbers, and the scanning step size. The imaging performance using different configurations in scattering media with different scattering coefficients are compared.

2. Methods

2.1. *Fluorescence laminar optical tomography (FLOT)*

In FLOT, an array of detectors is used with increasing separation from the source to capture light traveling through different depths (see Fig. 1). Depth-resolved FLOT images are obtained through image reconstruction similar to those used in CT or DOT.[14] The fluorescence signal from detector located at $\boldsymbol{r}_d$ can be expressed as[4,15]:

$$F_0(\vec{r}_d, \hat{\Omega}_d) = \frac{\sigma_{\text{ex}} \cdot \gamma}{4\pi} \int \psi_{\text{ex}}(\vec{r} - \vec{r}_s) \cdot C_f(\vec{r}) \cdot \psi_{\text{em}}(\vec{r}_d - \vec{r}\,) \cdot d^3\,\vec{r}\,, \quad (1)$$

where σ_{ex} is the absorption cross-section of the fluorophores at the excitation wavelength, γ is the fluorescence quantum yield, $\Psi_{\text{ex}}(\boldsymbol{r} - \boldsymbol{r}_s)$ is the excitation fluence distribution at position $\boldsymbol{r}$ from the excitation photon radiance source located at $\boldsymbol{r}_s$, $C_f(\boldsymbol{r})$ is the fluorophore concentration at position $\boldsymbol{r}$, and $\Psi_{\text{em}}(\boldsymbol{r}_d - \boldsymbol{r})$ is the probability that a photon emitted by a source at position $\boldsymbol{r}$ will be detected by a detector located at $\boldsymbol{r}_d$. Equation (1) can be discretized into voxels, which yields a matrix equation:

$$F = JC, \quad (2)$$

where F is the fluorescence measurements, C is the spatially-distributed fluorophores concentration, and J is the weight function matrix that represent the sensitivity of each measurement to the fluorophore concentration at each voxel and can be expressed as:

$$J_{s,m}(\vec{r}_s, \vec{r}_d, \vec{r}) = D_0 \cdot \psi_{\text{ex}}(\vec{r} - \vec{r}_s) \cdot \psi_{\text{em}}(\vec{r}_d - \vec{r}), \quad (3)$$

where D_0 is a constant number.

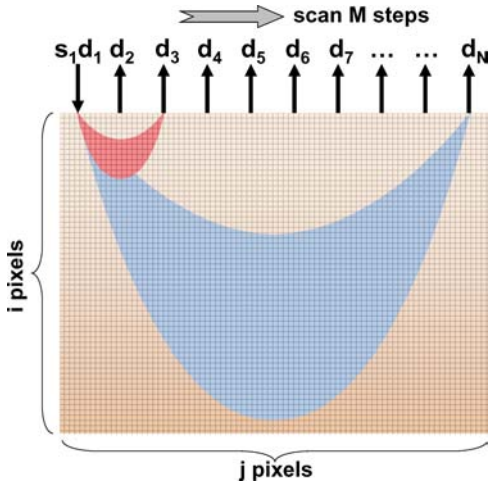

Fig. 1. Schematics of FLOT geometry used in this study. The optode arrangement is denoted by S (source) and d_n (array detectors, $n = 1 - N$). Different detectors collect photons traveling through different depths (as cartooned by red and blue shapes). The source-detector tandem is scanned M steps across the surface of medium resulting in a total number of measurements of $M \times N$. Field of view (FOV) is discretized by $i = 50$ pixels in depth and $j = 70$ pixels in the lateral direction. Pixel size is 30×30 μm^2, and the FOV is 1.5×2.1 mm^2.

2.2. *Monte Carlo simulation*

The sensitivity matrix J can be generated by either analytical or numerical methods.[1,16] Monte Carlo simulation is a widely-used method to generate the photon propagation profile in the scattering media.[17–21] In this study, we use the following specifications: field of view (FOV) is $i = 50$ pixels in depth (Z) by $j = 70$ pixels in the lateral direction (X), with pixel size of 30×30 μm^2, giving total FOV size equal to 1.5×2.1 mm^2. Y dimension is parallel to line illumination. Since emission wavelength is usually several tens of nanometers (nm) longer than excitation wavelength for many commonly used dye-based fluorophores, for simplicity, we assume

the scattering coefficients (μ_s) to be the same for both excitation and emission wavelengths, as was done in previous publications.[22] The scattering coefficient μ_s varies from 30−200 cm^{-1}, while the absorption coefficient $\mu_a = 10^{-3}$ cm^{-1} and the anisotropy factor $g = 0.84$ are kept the same. About 10^7 photons are launched in each source-detector configuration.

2.3. *Image reconstruction*

Equation (2) is then inverted so that the image C can be recovered from the measurements F and the weight matrix J. For a specific image configuration, weight matrix J is constructed by Monte Carlo simulation. Simulated measurement F is then generated by Eq. (2). To mimic realistic experimental conditions, 1.5% Gaussian noise is added in F. To reconstruct C, Tikhonov regularization is applied[2]:

$$C = (J^T \times J + \lambda^2 \times \text{Max}SV^2 \times I)^{-1} \times J^T \times F, \tag{4}$$

where MaxSV is the largest singular value in J and λ is the regularization factor that leverages the signal level and expected noise level. In this study, we choose $\lambda = 3 \times 10^{-4}$.

2.4. *Singular value analysis*

The matrix inversion in Eq. (4), however, is ill-posed so that the reconstructed image C is underdetermined and as a result non-unique. Understanding and then optimizing J is therefore critical to the reconstruction process. Singular value analysis (SVA) is a method to decompose the weight matrix (J) into an eigenvalue spectrum and has been applied to the optimization of DOT to achieve a favorable image resolution.[23,24] SVD of the weight matrix J yields a triplet of matrices $J = USV^T$. The magnitude of the singular values of S provides a measure of the relative effects of these image−space modes on the detected signal. The singular values are ordered to decrease in magnitude with increasing image−space mode indices.[2]

In this study, we use SVA to investigate the optimization of resolution and sensitivity by designing the optimal FLOT imaging configuration. The configurations considered here have four parameters: source incidence angle, detector detecting angle, detector sampling density, and source-detector scanning interval.

3. Results

3.1. *Singular value analysis of oblique angle configuration*

Figure 2 shows the sensitivity profiles (XZ) of FLOT for a representative source-detector pair based on Monte Carlo simulation. Configurations with 0° (top row) and 30° (bottom row) incidence and detection angles show distinct sensitivity pattern. For convenience, we start with symmetric configuration with the same incidence and detection angles. For each configuration, different scattering coefficients ($\mu_s = 50, 100$, and 150 cm^{-1}) are chosen as the background medium (left to right). The sensitivity map indicates the probability density of photons delivered to each location by the source and captured by the detector. Photon paths appear more ballistic for low-scattering medium ($\mu_s = 50$ cm^{-1}) while they become more scattered in high-scattering medium ($\mu_s = 150$ cm^{-1}). Similar trends are observed for other source-detector pairs (data not shown).

Weight matrix (J) is then composed by many different sensitivity profiles. Each profile is a measurement configuration. Here, each profile (XZ) contains $70 \times 50 = 3500$ pixels as mentioned in Sec. 2.2, and there are 70 source-detector separations and 70 scanning positions, giving 4900 measurements. Matrix J is therefore of size 4900×3500. Singular value decomposition (SVD) of the weight matrix J provides the singular values (SVs) indicating the relative effects of different image-space modes on the detected signal. In this part of study, we first tune the angle of source incidence and detector collection. For convenience, both angles are set equal for now. A set of SVs of J are generated for each angle from 0° to 50° with 10° increment and plotted in Figs. 3(a)−3(c). Figures 3(a)−3(c) correspond to different background scattering coefficients ($\mu_s = 50, 100, 150$ cm^{-1}, respectively). The threshold for the singular value analysis is set to $10^{-3.6}$ (corresponding to the dynamic range of detector). The number of singular values above the threshold represents a measure of the useful information contained in that data for image reconstruction. Figure 3(d) plots the number of useful SVs above the threshold for different scattering coefficients. The 30° configuration

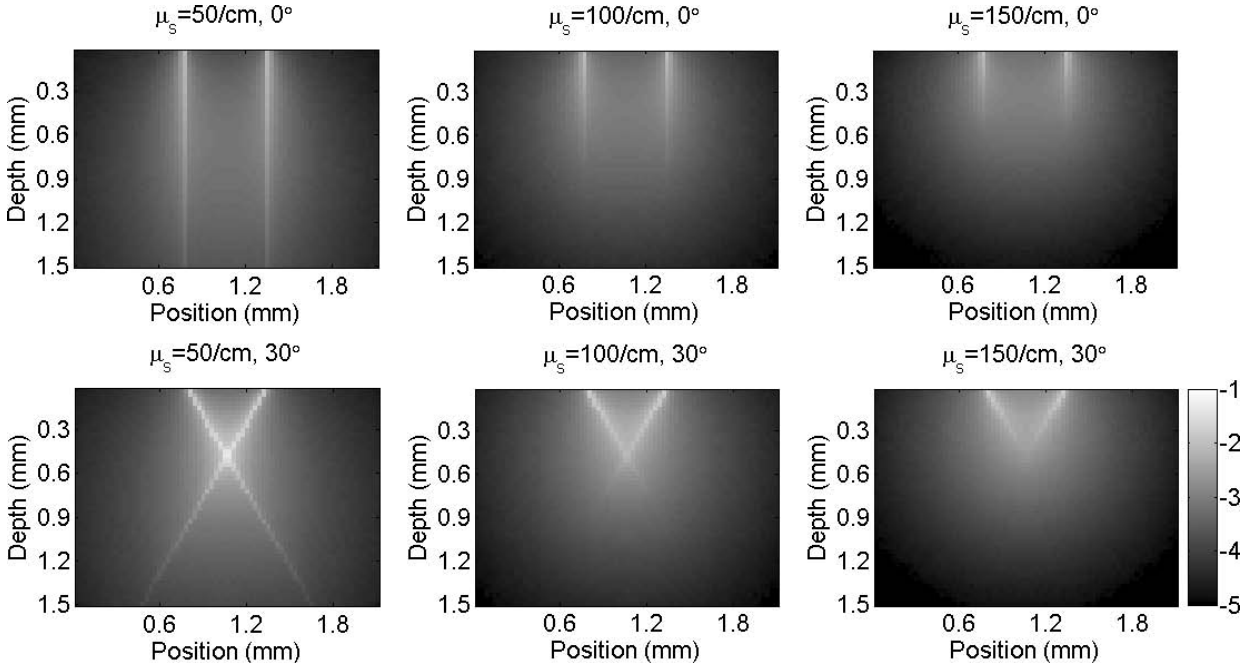

Fig. 2. Sensitivity maps (in log10 scale) for one source-detector pair with 0° (top row) and 30° (bottom row) incidence/detection angles. For each configuration, different scattering coefficients ($\mu_s = 50$, 100, and 150 cm^{-1}) is specified for the medium (left to right). The sensitivity map (plotted in log 10 scale) indicates the probability density of photons delivered to the location by the source and captured at the location by the detector.

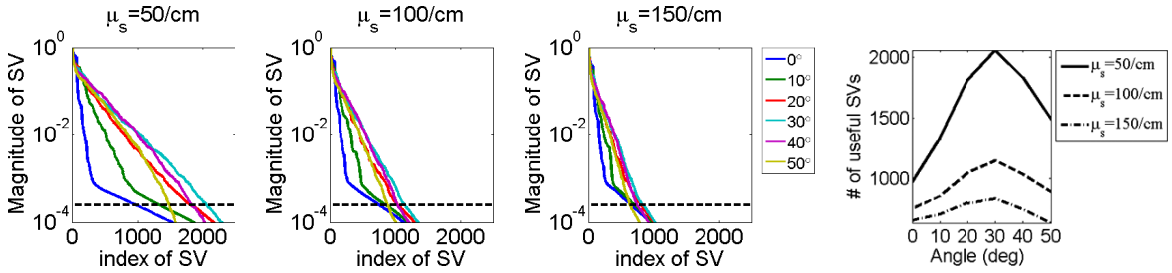

(a) (b) (c) (d)

Fig. 3. Comparison of singular value (SV) distributions among different incidence/detection angles. For convenience, same incidence and detection angels are specified. (a) SV distribution for $\mu_s = 50$ cm^{-1}; (b) SV distribution for $\mu_s = 100$ cm^{-1}; and (c) SV distribution for $\mu_s = 150$ cm^{-1}. Detection threshold is specified as $10^{-3.6}$. Only SV above the threshold carries useful information for image reconstruction. (d) Plot of the number of useful SV (above the threshold).

excels among other angles in the sense of having the highest number of useful SVs, especially in low scattering medium ($\mu_s = 50$ cm^{-1}).

Figure 4(a) plots the number of useful SVs (k) versus the background medium scattering coefficient from 30−200 cm^{-1} and for 0° and 30° configurations. The ratio of 30°'s number of useful SV to that of 0° (k_{30}/k_0) is plotted in Fig. 4(b). For lower scattering medium, k_{30} is approximately 2.5 times larger than k_0, suggesting 30° configuration has improved performance over 0° configuration. As μ_s increases, the ratio approaches 1, indicating that the performance between these two configurations becomes comparable.

3.2. *Imaging performance of oblique angle configuration*

To validate the prediction from singular value analysis, we perform image reconstruction of a point object (with intensity equal to 1) under different configurations. The point spread function along axial (z) direction through the position of point object is plotted versus the depth of the object,

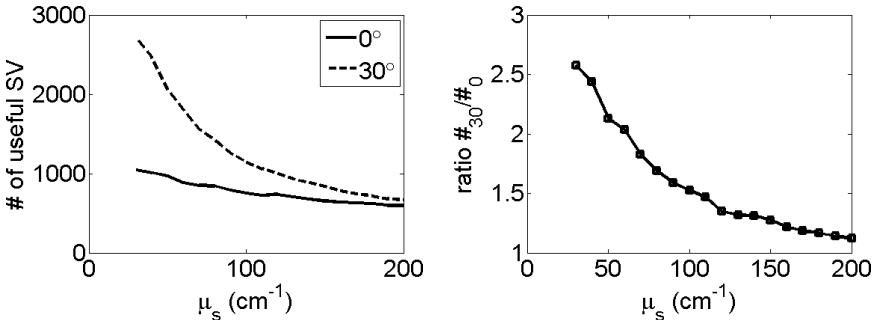

(a) (b)

Fig. 4. (a) The number of useful SVs (k) versus scattering coefficient from 30 to 200 cm^{-1} for 0° and 30° configurations. (b) The ratio of 30°'s number of useful SV to that of 0° (k_{30}/k_0).

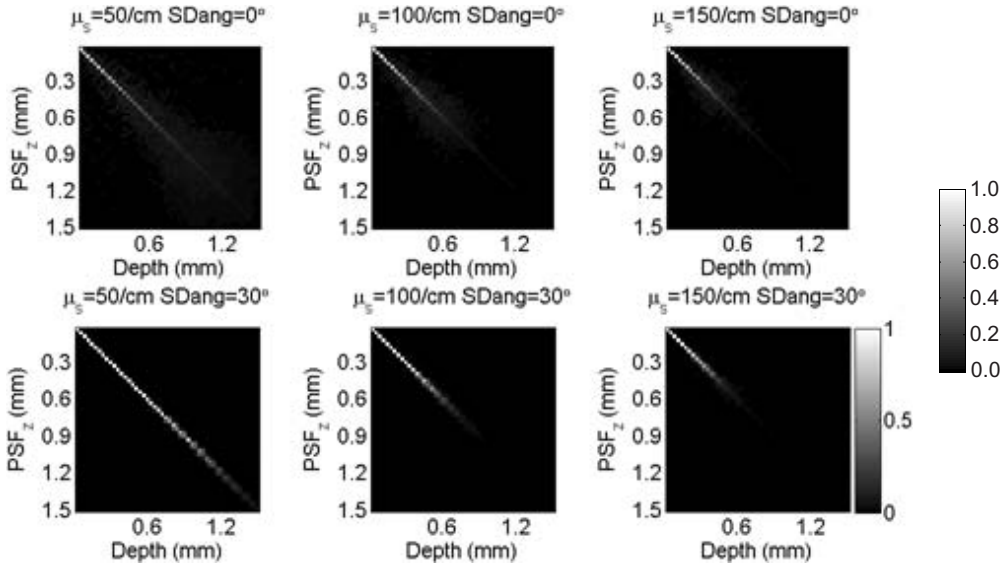

Fig. 5. Axial (z-direction) point spread functions (PSF_z) versus depth (z). PSF_z is generated by placing a point object (with intensity equal to 1) at various depths in the center of the FOV. The center column of the reconstructed FOV represents PSF_z and is plotted along with different object position. Representative results from 0° (top row) and 30° (bottom row) configurations and different scattering coefficients ($\mu_s = 50, 100$, and 150 cm^{-1}, left to right) are presented.

as shown in Fig. 5. Representative results from 0° (top row) and 30° (bottom row) configurations and different scattering coefficients ($\mu_s = 50, 100$, and 150 cm^{-1}, left to right) are presented. From the reconstruction, axial point spread function (PSF_z) broadens and its peak intensity decreases as the object goes deeper.

The details of PSF_z are analyzed using two parameters: (1) the reconstructed peak intensity (or depth sensitivity); and (2) the interquartile range (IQR). IQR represents the range that bounds an area of 50% centered around the median value under the PSF curve. IQR is a more stable estimate of spread than full-width-at-half-maximum (FWHM) in the presence of long tail distribution.[22]

Figure 6 shows the PSF_z peak intensity (or depth sensitivity) derived from Fig. 5 versus depth for different configurations. In general, at a given depth, 30° configuration has higher peak intensity (sensitivity) than 0° configuration, especially in the shallower depth region. The difference becomes less prominent for high scattering medium ($\mu_s =$ 150 cm^{-1}). It is interesting, however, that when normalizing these sensitivity curves to mean free path (MFP) ($1/\mu_s$) (i.e., replacing d with $\mu_s d$ in x-axis of the plot), only 30° configurations grouped together, as shown in Fig. 6(d). The fact that normal configurations are not unified indicates that the underlying mechanisms between angled and normal configurations are different as photons

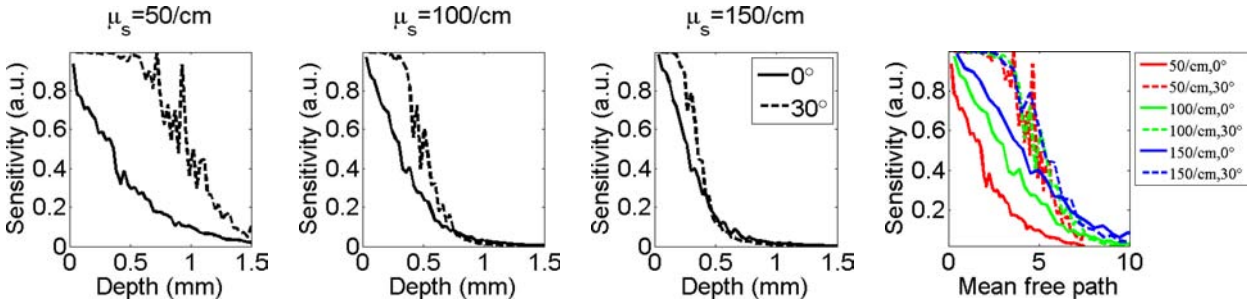

(a) (b) (c) (d)

Fig. 6. PSF_z peak intensity (derived from Fig. 5) versus depth for different configurations. (a) $\mu_s = 50\ cm^{-1}$; (b) $\mu_s = 100\ cm^{-1}$; (c) $\mu_s = 150\ cm^{-1}$; and (d) normalized to mean free path.

significantly rely on backscattering to travel from source to detector in normal configurations, while the incidence and detection paths overlap in angled configurations.

Figure 7 plots the IQR of PSF_z derived from Fig. 5 versus depth for different configurations. In general, 30° configuration has smaller IQR (higher axial resolution) than 0° configuration. Especially, in low scattering medium ($\mu_s = 50\ cm^{-1}$), IQR for 30° configuration remains ~ 30 μm up to 1 mm, and remains <100 μm up to 1.5 mm. In contrast, IQR for 0° configuration increases rapidly to ~400 μm at 1 mm. However, the difference between these two configurations becomes less prominent as the background scattering increase, and the IQRs for both configurations are almost identical for high scattering medium ($\mu_s = 150\ cm^{-1}$). Again, when normalizing to MFP as shown in Fig. 7(d), the grouping of the curves was observed. However, different from the sensitivity, the grouping (unifying) of IQR curves occurred at both normal and angled configurations, which is expected because both IQR and MFP are in terms of distance. This also indicates that IQR and sensitivity provide inherently different measures.

In previous analysis, we set both the source incidence and detector collection angles the same. In practice, both angles may vary independently. Figure 8 shows the number of useful SVs versus the incidence and detection angles for different μ_s values. In general, the combination of source incidence angle of $\leq 20°$ and detection angle of $\geq 30°$ yields the optimal number of useful SVs, therefore suggesting a better imaging performance. However, the enhancement from 0° configuration degrades when the background scattering coefficient increases ($k_{max}/k_0 = 2.5$ for $\mu_s = 50\ cm^{-1}$; 1.6 for $\mu_s = 100\ cm^{-1}$; 1.4 for $\mu_s = 150\ cm^{-1}$). These results suggest the enhancement via angled incidence/detection is more dramatic in lower scattering medium.

3.3. *Effects of different detector numbers*

Figure 9 shows the number of useful SVs versus the number of detectors (from 7 to 70) for different μ_s

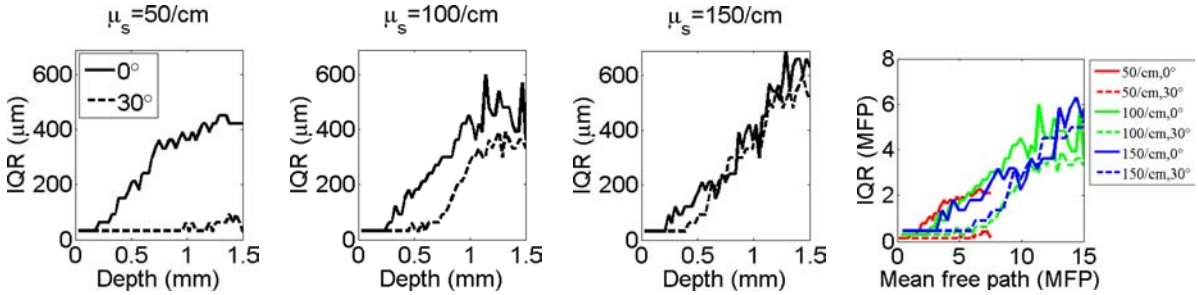

(a) (b) (c) (d)

Fig. 7. PSF_z interquartile range (IQR) (derived from Fig. 5) versus depth for different configurations. (a) $\mu_s = 50\ cm^{-1}$; (b) $\mu_s = 100\ cm^{-1}$; (c) $\mu_s = 150\ cm^{-1}$; and (d) normalized to mean free path.

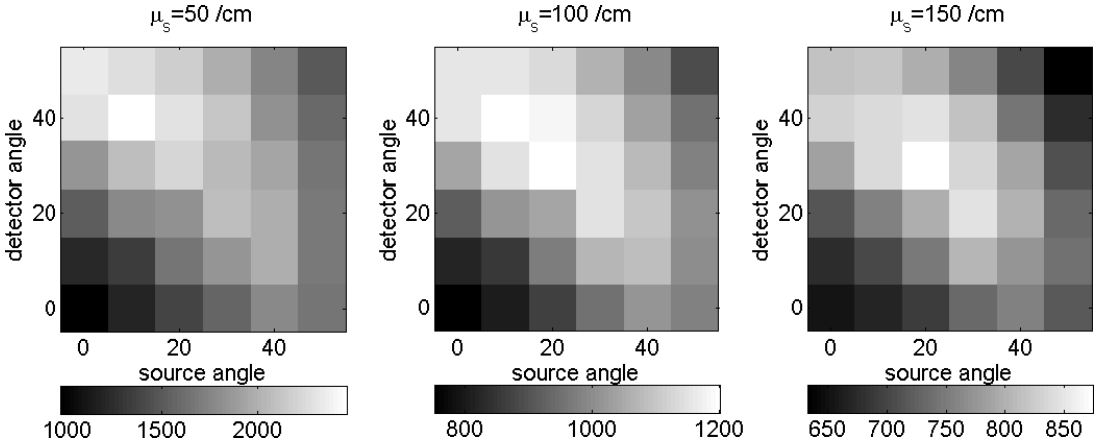

Fig. 8. The number of useful SVs versus the incidence and detection angles for different μ_s values.

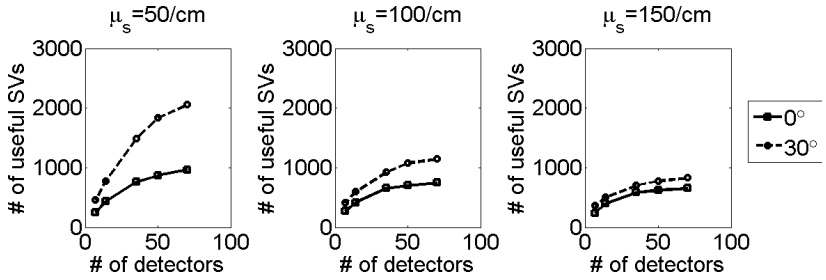

Fig. 9. The number of useful SVs versus the number of detectors for different μ_s values.

values. In general, the more detector numbers, the more useful SVs. The increase is most prominent for 30° configuration in low-scattering medium ($\mu_s = 50\ \text{cm}^{-1}$) and becomes less dramatic in high-scattering medium ($\mu_s = 150\ \text{cm}^{-1}$).

Figure 10 shows the peak intensity (or depth sensitivity) derived from the reconstructed PSF_z versus depth for different detector numbers. Increasing the number of detectors from 7 to 35 generally increases the depth sensitivity, for both 0°

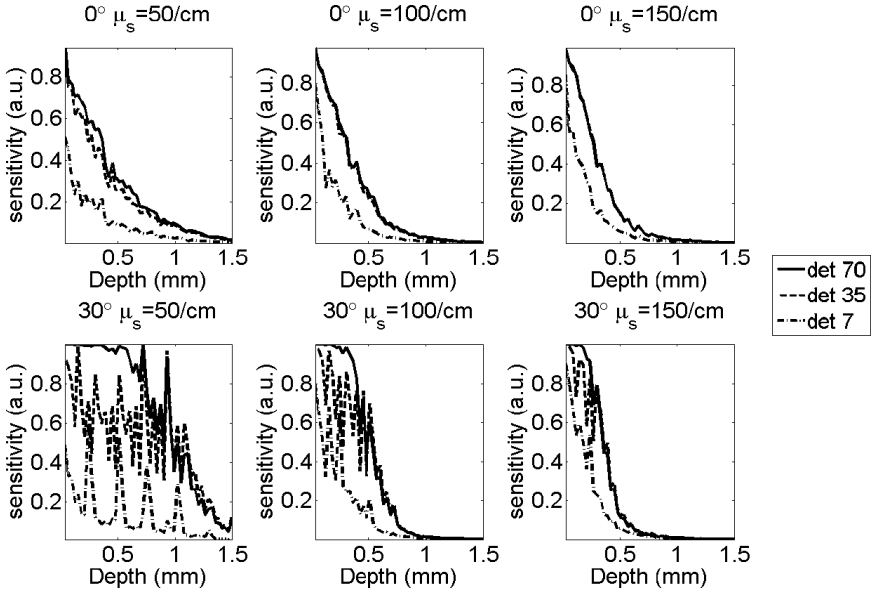

Fig. 10. The peak intensity (derived from PSF_z) versus depth for different detector numbers.

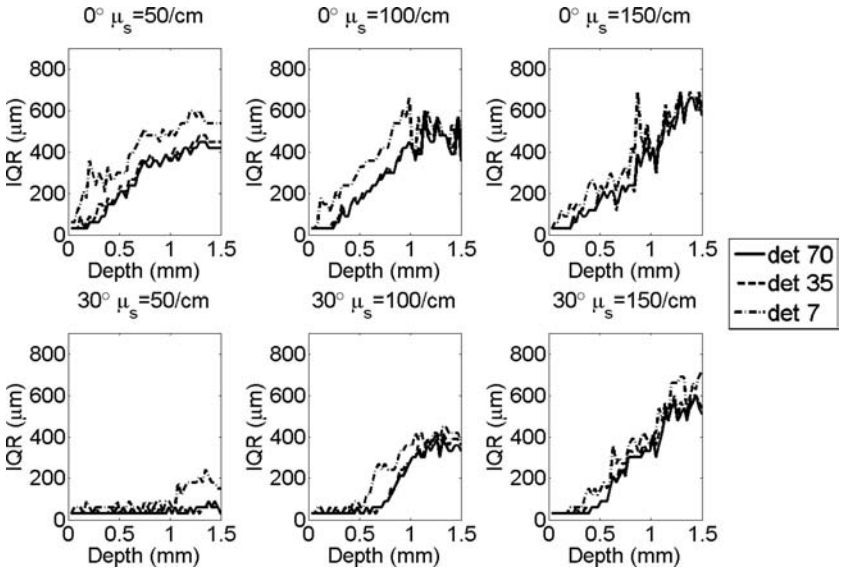

Fig. 11. IQR (derived from PSF_z) versus depth for different detector numbers.

and 30° configurations. The 30° angled incidence/detection (bottom row) further increases the sensitivity at deeper depths. The difference between 35 detectors and 70 detectors is less apparent, especially in high-scattering medium. There are some spikes present in 30° angled incidence/detection, which are due to the undersampling effects (will be discussed in Sec. 3.5).

Figure 11 shows the IQR derived from PSF_z versus depth for different detector numbers. Increasing the number of detectors generally decreases the width of PSF_z (improves axial resolution). The 30° angled incidence/detection configuration dramatically decreases IQR (improves axial resolution), especially in low-scattering medium ($\mu_s = 50$ cm^{-1}). Lower detector number (7) shows larger axial resolution than those use more detectors, especially in the cases of $\mu_s = 50$ and 100 cm^{-1}. The difference between 35 and 70 detectors is less apparent. In high-scattering medium ($\mu_s = 150$ cm^{-1}), the IQRs of 7, 35, and 70 detectors are comparable, in both 0° and 30° configurations.

3.4. *Effects of scanning steps*

Figure 12 shows the number of useful SVs versus the step sizes of scanning for different μ_s values. Smaller step size (denser sampling) is associated with more useful SVs, and hence more useful information for reconstruction. The effect is more prominent in 30° angled incidence/detection configuration with low-scattering medium ($\mu_s = 50$ cm^{-1}) and becomes less dramatic in high-scattering medium ($\mu_s = 150$ cm^{-1}).

Figure 13 shows the peak intensity (or depth sensitivity) derived from the reconstructed PSF_z versus depth for different step sizes of scanning. The number of detectors is kept the same (70) in all

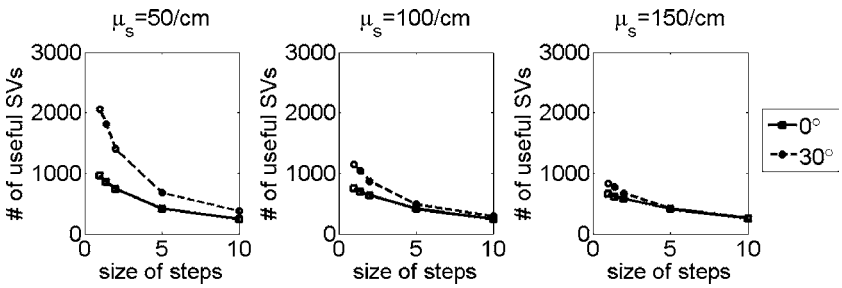

Fig. 12. The number of useful SVs versus the step sizes of scanning for different μ_s values. Smaller step size (unit: pixel) is associated with larger useful SV number, and hence more useful information for reconstruction.

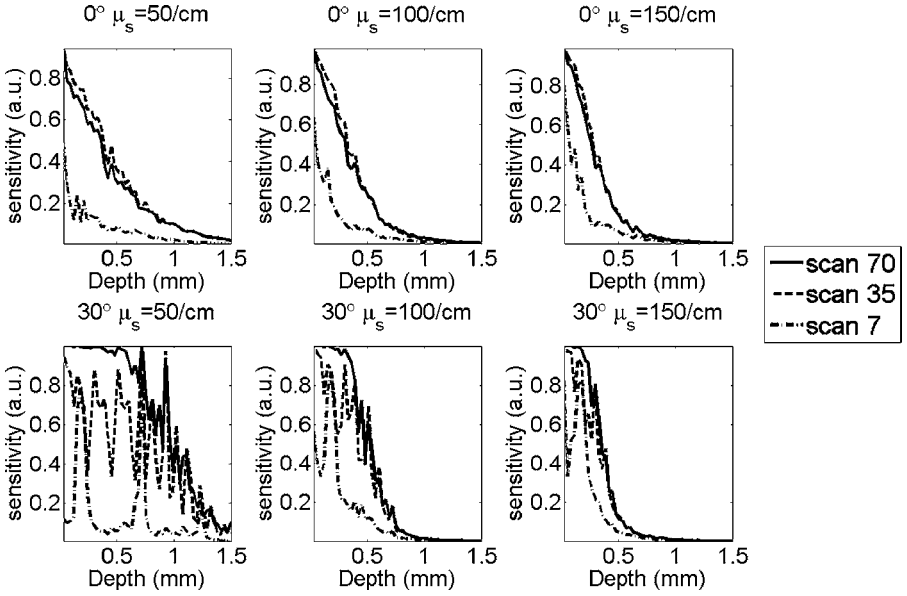

Fig. 13. The peak intensity (derived from PSF_z) versus depth for different step sizes of scanning. The number of detectors is kept the same (70) in all cases.

cases. Reducing the step size (denser sampling) generally increases the sensitivity; 35 scans (with step size of 2 pixel) are comparable with 70 scans (with step size of 1 pixel), and both outperform 7 scans (with step size of 10 pixel) in 0° configuration (top row). The 30° angled incidence/detection (bottom row) enhances the sensitivity at deeper depths. Again, both 35 and 70 scans outperform 7 scans. Periodic peaks are present due to the undersampling effects (will be discussed in Sec. 3.5).

Figure 14 shows the IQR derived from the reconstructed PSF_z versus depth for different step sizes of scanning. The number of detectors is kept the same (70) in all cases. Reducing the step size (denser sampling) generally decreases IQR (improves axial resolution); 35 scans (with step size

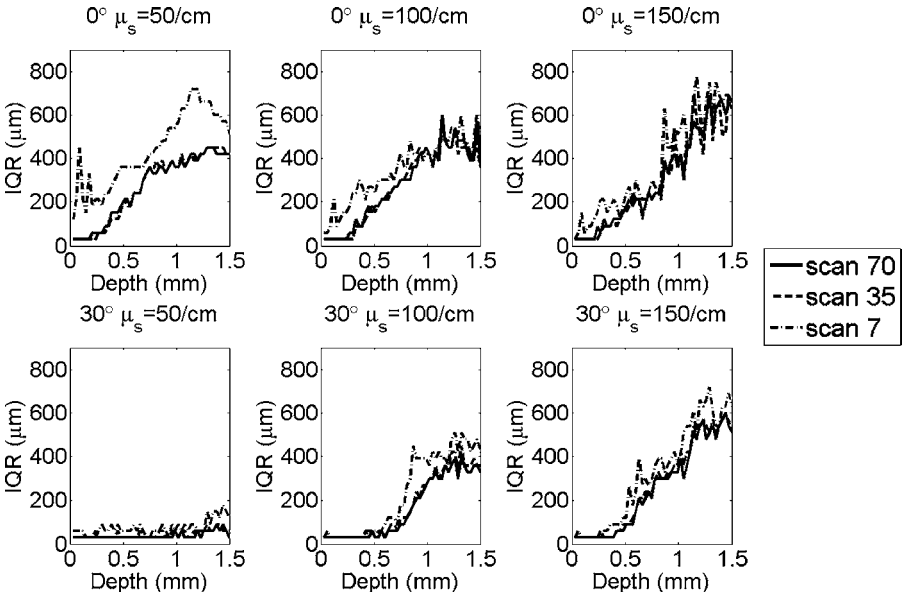

Fig. 14. IQR (derived from PSF_z) versus depth for different step sizes of scanning. The number of detectors is kept the same (70) in all cases.

of 2) are comparable with 70 scans (with step size of 1), and both outperform 7 scans (with step size of 10) in 0° configuration (top row) and 30° angled incidence/detection (bottom row), especially in low-scattering medium ($\mu_s = 50$ cm^{-1}). The IQRs of 7, 35, and 70 scans are comparable in high-scattering medium ($\mu_s = 150$ cm^{-1}).

3.5. *Effects of angle, detector number, and scanning steps*

Figure 15 shows the peak sensitivity map over the entire FOV for $\mu_s = 50$ cm^{-1}, with both 0° and 30° configurations. The sensitivity map is generated by placing a point object (with unit intensity) at each position (i, j) within the FOV and obtain the reconstructed value at (i, j). In general, increasing detector numbers and scan steps can increase the sensitivity at deeper region, and achieve a more uniform reconstruction. Undersampling is more prominent when scanning steps are sparse ($S = 7$). Grid patterns appear in $[D, S] = 7, 7$ in Fig. 15(b), for instance, explain the periodic peaks in Figs. 10 and 13. For low detector number ($D = 7$), 30° configuration is more vulnerable to undersampling effect than 0° configuration. Increasing the scattering coefficient (as shown in Figs. 16 and 17) results in less severe undersampling effect, as the photon path becomes more diffusive rather than ballistic. In addition, penetration depth (regions with high sensitivity) becomes shallower because of increased scattering.

4. Discussion

To optimize FLOT imaging, we perform singular value analysis (SVA) to investigate the impact of source-detector configuration on imaging performance, including axial resolution and depth sensitivity. We use Monte Carlo simulation to generate photon sensitivity matrices with different incidence/detection geometry, detector numbers, and scanning steps. SVA is performed on the respective weight matrix to compare the singular value distributions among different configurations. Configurations with larger number of singular values above the detection noise indicate more information contents can be acquired, and thereby, suggesting the potential of improvement on FLOT imaging.

Our results show that using angled incidence and detection could improve the resolution and depth sensitivity for FLOT, especially for lower scattering medium. In this study, for simplicity, we mostly focus on the symmetric configuration where the incidence and detection angles are equal. Our results indicate that the optimal configuration can be achieved when both the incidence and detection angles are 30°, which outperforms normal incidence and detection, as in conventional FLOT design. The optimal combination of incidence and detection angles can be investigated in a similar way. Depending on the background scattering, the optimal angle pair may change (see Fig. 8). As scattering increases, for example, to $\mu_s \sim 150$ cm^{-1}, the enhancement of angled configuration over normal configuration is less prominent.

To explain the enhancement of probing depth for angled configuration at low scattering ($\mu_s \sim 50$ cm^{-1}), we can consider two extreme scenarios. On one hand, at very high scattering situations, the photons undergo strong multiple scattering and behave as diffusion. In this case, the incidence and detection angles play little role, therefore, the probing depths of these two configurations (0° and 30°) are comparable, as shown in Figs. 6 and 7 (with $\mu_s = 150$ cm^{-1}). On the other hand, when the sample has no scattering (transparent), normal incidence and detection will never detect signals (zero backscattering) when the detector is away from the source position. However, angled incidence and detection configuration can still detect deep object as long as it is covered by the farthest detector away from the source, therefore the probing depth is deeper. In realistic situations, tissue scattering coefficients usually fall between these two extremes, therefore the probing depth for angled configuration enhances to various degree depending on tissue scattering coefficients.

In this study, we also vary the detector numbers (from 7 to 70) and scanning steps (from 7 to 70). We find that the increase of the number of detectors and the number of scanning steps will result in the presence of more useful singular values, which promises to enhance the imaging performance. For an FOV discretized to 50 by 70 pixels, reducing the detector numbers to 35, and downsampling to 35 steps (i.e., $[D, S] = 35, 35$ in Figs. 15–17) still maintain reasonable reconstruction, especially for higher scattering cases. However, low detector numbers ($D = 7$) and low sampling steps ($S = 7$) might result in undersampling for the specified FOV and pixel size, which in turn reduces the resolution. But the impacts of low detector number and low

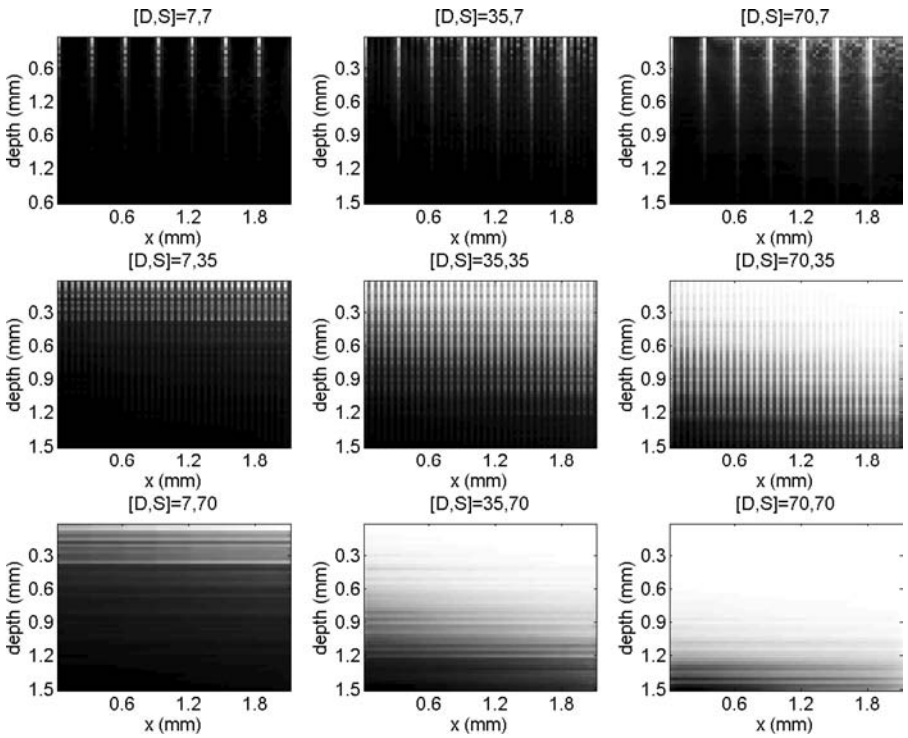

(a)

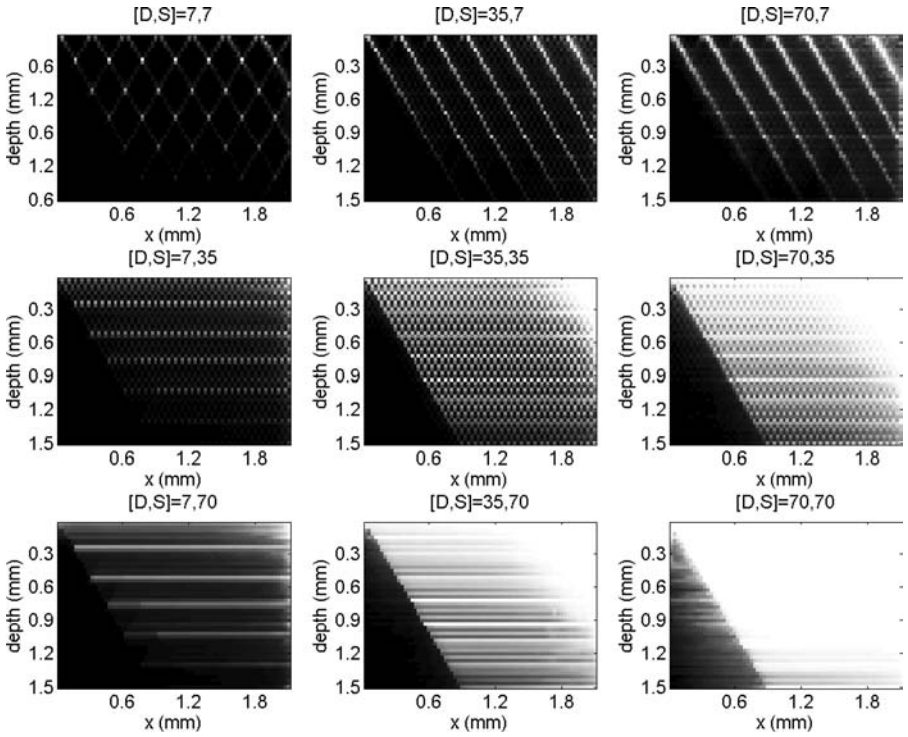

(b)

Fig. 15. Peak sensitivity map of FOV for $\mu_s = 50$ cm^{-1}. (a) 0° configuration, and (b) 30° configuration. $[D, S]$ denotes the number of detectors and scan steps. The sensitivity map is generated by placing a point object (with unit intensity) at each position (i, j) within the FOV and obtain the reconstructed value at (i, j).

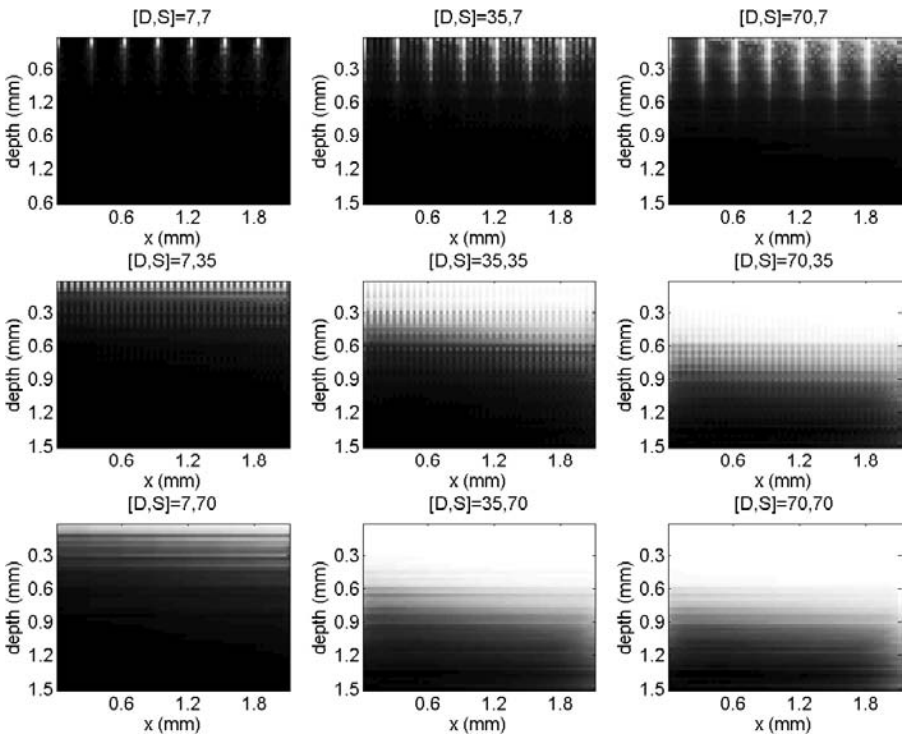

(a)

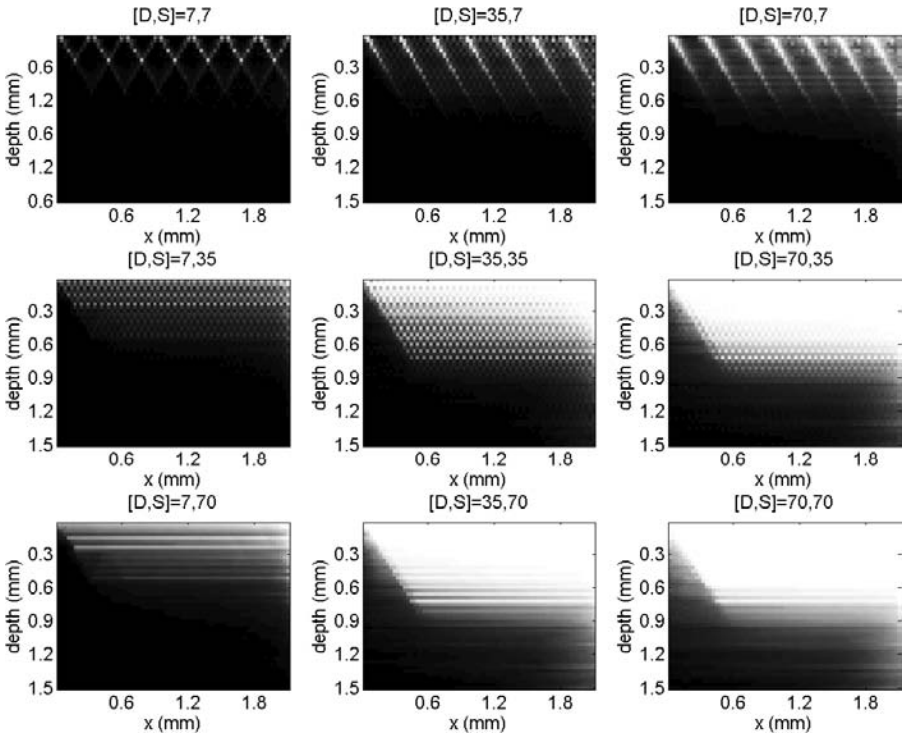

(b)

Fig. 16. Peak sensitivity map of FOV for $\mu_s = 100\ \mathrm{cm}^{-1}$. (a) 0° configuration, and (b) 30° configuration. [D, S] denotes the number of detectors and scan steps.

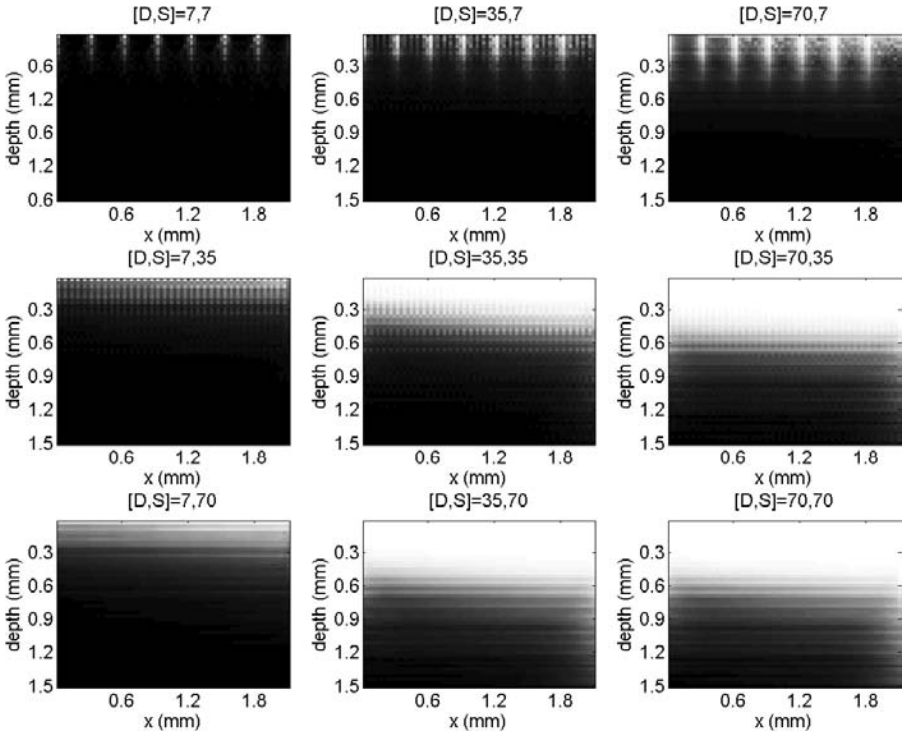

(a)

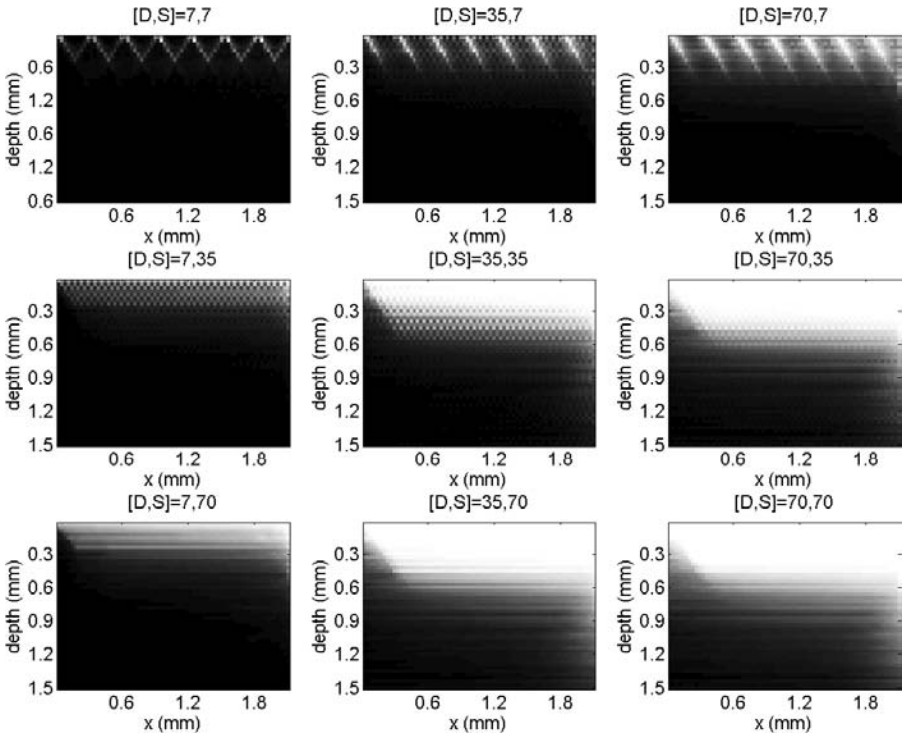

(b)

Fig. 17. Peak sensitivity map of FOV for $\mu_s = 150\ \mathrm{cm}^{-1}$. (a) 0° configuration, and (b) 30° configuration. [*D*, *S*] denotes the number of detectors and scan steps.

Table 1. Scattering coefficients at the excitation and emission wavelengths of several commonly used dyes for 2% Intralipid (calculated based on Ref. 25).

Dye	λ_{ex} (nm)	λ_{em} (nm)	μ_s at λ_{ex} (cm^{-1})	μ_s at λ_{em} (cm^{-1})
Fluorescein	494	518	123.8	110.9
Rhodamine B	570	590	88.7	81.9
Cy5.5	675	695	59.8	55.9
ICG	780	805	42.7	39.7

sampling steps are not equivalent. Low sampling steps ($S = 7$) inevitably result in undersampling effect within the FOV (first row, $S = 7$, in Figs. 15–17), but low detector numbers ($D = 7$) might still be sufficient to reconstruct the object without obvious undersampling effect, especially for high-scattering media (first column, $D = 7$, in Figs. 16 and 17). In principle, the number of detectors relates to the axial resolution and the steps of sources relate to the transverse resolution.

In this study, we focus on optimization of FLOT imaging. For simplicity, we assume the scattering coefficient in both the excitation and emission wavelengths are the same. Since the Stokes shifts (the difference between the excitation and emission wavelengths) are different for different fluorophores, hence the differences in the scattering coefficients at excitation and emission wavelengths might vary case by case. However, usually the Stokes shifts are small (several tens of nm) for many organic dyes commonly used in biological imaging, and therefore the difference in the scattering coefficients are not dramatic. Table 1 lists the scattering coefficients for 2% Intralipid (a commonly used scattering phantom with scattering properties similar to human tissues[25]) at typical excitation and emission wavelengths for several commonly used fluorophores. The differences between the scattering coefficients at the excitation and emission wavelengths are small. To simplify the analysis, we choose the same μ_s values for both wavelengths to demonstrate the methodology. Similar analysis can be applied with modified μ_s values to reflect the actual situation when analyzing a specific case. In addition, from Table 1, with the increase of wavelength (especially in the near-infrared range), the tissue scattering coefficient decreases (down to low-scattering range $\sim 50\ cm^{-1}$). Therefore, enhancement from FLOT configuration optimization could be more evident. Furthermore, although we focus on FLOT optimization in this study, the analysis presented in this paper could be applied to LOT imaging as well.

5. Conclusion

In summary, we analyze several key design parameters in FLOT (including source/detector angles, detector numbers, and scanning steps) to optimize the imaging configuration. Our results indicate that angled incidence/detection configuration might improve the imaging resolution and depth sensitivity, especially for low-scattering medium. Increasing the number of detectors and the number of scanning steps will also result in enhanced imaging performance. We also demonstrate that the optimal imaging performance depends upon the background scattering coefficient. In high-scattering medium, the enhancement from optimizing those parameters is less prominent compared to low-scattering medium. Our result might provide an optimization strategy for FLOT or LOT experimental setup.

Acknowledgments

We acknowledge Dr. David Boas from Massachusetts General Hospital (MGH) for providing the Monte Carlo simulation code (tmcimg), and Drs. Heng Lian (Nanyang Technological University, Singapore), Quan Zhang (MGH), Qianqian Fang (MGH) for technical assistance in modifying the code. YC thanks Dr. Britton Chance for stimulating discussions and encouragement on FLOT technology development and biomedical applications. This work is supported in part by the Nano-Biotechnology Award of the State of Maryland, the Minta Martin Foundation, the General Research Board (GRB) Award of the University of Maryland, the University of Maryland Baltimore (UMB) and College Park (UMCP) Seed Grant Program, the Prevent Cancer Foundation.

References

1. A. Dunn, D. Boas, "Transport-based image reconstruction in turbid media with small source-detector separations," *Opt. Lett.* **25**, 1777−1779 (2000).
2. E. M. Hillman, D. A. Boas, A. M. Dale, A. K. Dunn, "Laminar optical tomography: Demonstration of millimeter-scale depth-resolved imaging in turbid media," *Opt. Lett.* **29**, 1650−1652 (2004).
3. S. A. Burgess, M. B. Bouchard, B. H. Yuan, E. M. C. Hillman, "Simultaneous multiwavelength laminar optical tomography," *Opt. Lett.* **33**, 2710−2712 (2008).
4. E. M. C. Hillman, O. Bernus, E. Pease, M. B. Bouchard, A. Pertsov, "Depth-resolved optical imaging of transmural electrical propagation in perfused heart," *Opt. Express* **15**, 17,827−17,841 (2007).
5. B. H. Yuan, S. A. Burgess, A. Iranmahboob, M. B. Bouchard, N. Lehrer, C. Bordier, E. M. C. Hillman, "A system for high-resolution depth-resolved optical imaging of fluorescence and absorption contrast," *Rev. Sci. Instrum.* **80**, 043706 (2009).
6. S. Yuan, Q. Li, J. Jiang, A. Cable, Y. Chen, "Three-dimensional coregistered optical coherence tomography and line-scanning fluorescence laminar optical tomography," *Opt. Lett.* **34**, 1615−1617 (2009).
7. Y. Chen, S. Yuan, J. Wierwille, R. Naphas, Q. Li, T. R. Blackwell, P. T. W. Jr., V. Raman, K. Glunde, "Integrated optical coherence tomography (OCT) and fluorescence laminar optical tomography (FLOT)," *IEEE Journal of Selected Topics in Quantum Electronics* **16**, 755−766 (2010).
8. C. F. Zhu, Q. Liu, N. Ramanujam, "Effect of fiber optic probe geometry on depth-resolved fluorescence measurements from epithelial tissues: A Monte Carlo simulation," *J. Biomed. Optics* **8**, 237−247 (2003).
9. T. J. Pfefer, A. Agrawal, R. A. Drezek, "Oblique-incidence illumination and collection for depth-selective fluorescence spectroscopy," *J. Biomed. Optics* **10**, 044016 (2005).
10. L. Nieman, A. Myakov, J. Aaron, K. Sokolov, "Optical sectioning using a fiber probe with an angled illumination-collection geometry: Evaluation in engineered tissue phantoms," *Appl. Opt.* **43**, 1308−1319 (2004).
11. Q. Liu, N. Ramanujam, "Experimental proof of the feasibility of using an angled fiber-optic probe for depth-sensitive fluorescence spectroscopy of turbid media," *Opt. Lett.* **29**, 2034−2036 (2004).
12. M. C. Skala, G. M. Palmer, C. F. Zhu, Q. Liu, K. M. Vrotsos, C. L. Marshek-Stone, A. Gendron-Fitzpatrick, N. Ramanujam, "Investigation of fiber-optic probe designs for optical spectroscopic diagnosis of epithelial pre-cancers," *Laser Surg. Med.* **34**, 25−38 (2004).
13. S. D. Konecky, G. Y. Panasyuk, K. Lee, V. Markel, A. G. Yodh, J. C. Schotland, "Imaging complex structures with diffuse light," *Opt. Express* **16**, 5048−5060 (2008).
14. S. R. Arridge, "Optical tomography in medical imaging," *Inverse Problems* **15**, R41−R93 (1999).
15. R. J. Crilly, W. F. Cheong, B. Wilson, J. R. Spears, "Forward-adjoint fluorescence model: Monte Carlo integration and experimental validation," *Appl. Optics* **36**, 6513−6519 (1997).
16. B. H. Yuan, "Radiative transport in the Delta-P1 approximation for laminar optical tomography," *J.I.O.H.S.* **2**, 149−163 (2009).
17. S. T. Flock, M. S. Patterson, B. C. Wilson, D. R. Wyman, "Monte Carlo modeling of light propagation in highly scattering tissues. I. Model predictions and comparison with diffusion theory," *IEEE Transactions on Biomedical Engineering* **36**, 1162−1168 (1989).
18. L. H. Wang, S. L. Jacques, L. Q. Zheng, "Mcml — Monte Carlo modeling of light transport in multi-layered tissues," *Comp. Meth. Prog. Biomed.* **47**, 131−146 (1995).
19. J. Barton, T. E. Milner, T. J. Pfefer, J. S. Nelson, A. J. Welch, "Optical low-coherence reflectometry to enhance Monte Carlo modeling of skin," *J. Biomed. Opt.* **2**, 226−234 (1997).
20. G. Yao, L. V. Wang, "Monte Carlo simulation of an optical coherence tomography signal in homogeneous turbid media," *Phys. Med. Biol.* **44**, 2307−2320 (1999).
21. D. A. Boas, J. P. Culver, J. J. Stott, A. K. Dunn, "Three-dimensional Monte Carlo code for photon migration through complex heterogeneous media including the adult human head," *Opt. Express* **10**, 159−170 (2002).
22. A. A. Tanbakuchi, A. R. Rouse, A. F. Gmitro, "Monte Carlo characterization of parallelized fluorescence confocal systems imaging in turbid media," *J. Biomed. Opt.* **14**, 044024 (2009).
23. J. P. Culver, V. Ntziachristos, M. J. Holboke, A. G. Yodh, "Optimization of optode arrangements for diffuse optical tomography: A singular-value analysis," *Opt. Lett.* **26**, 701−703 (2001).
24. E. E. Graves, J. P. Culver, J. Ripoll, R. Weissleder, V. Ntziachristos, "Singular-value analysis and optimization of experimental parameters in fluorescence molecular tomography," *J. Optics Soc. America a-Optics Image Science and Vision* **21**, 231−241 (2004).
25. S. T. Flock, S. L. Jacques, B. C. Wilson, W. M. Star, M. J. C. Vangemert, "Optical-properties of intralipid — A phantom medium for light-propagation studies," *Laser Surg. Med.* **12**, 510−519 (1992).